

## Graphical Abstract

### **Accelerated Diffusion Magnetic Resonance Imaging at 7 T: Joint Reconstruction for Multi-Shell Multi-Band Shift-Encoded Echo Planar Imaging (JETS-EPI)**

Zhengguo Tan, Patrick Alexander Liebig, Robin Martin Heidemann, Frederik Bernd Laun, Florian Knoll

## Highlights

### Accelerated Diffusion Magnetic Resonance Imaging at 7 T: Joint Reconstruction for Multi-Shell Multi-Band Shift-Encoded Echo Planar Imaging (JETS-EPI)

Zhengguo Tan, Patrick Alexander Liebig, Robin Martin Heidemann, Frederik Bernd Laun, Florian Knoll

- Novel accelerated diffusion acquisition with shifted phase encoding among diffusion directions for complementary  $k$ - $q$ -space sampling at 7 T
- Generalized joint  $k$ - $q$ -slice diffusion-weighted image reconstruction with overlapping locally low-rank regularization
- 5 min 1.2 mm isotropic resolution with  $b$ -value 1000 s/mm<sup>2</sup> for in vivo whole-brain diffusion tensor imaging
- 23 min 1 mm isotropic resolution with three-shell high  $b$ -values (up to 3000 s/mm<sup>2</sup>) for in vivo whole-brain diffusion tensor imaging and fiber tracking



# Accelerated Diffusion Magnetic Resonance Imaging at 7 T: Joint Reconstruction for Multi-Shell Multi-Band Shift-Encoded Echo Planar Imaging (JETS-EPI)

Zhengguo Tan<sup>a</sup>, Patrick Alexander Liebig<sup>b</sup>, Robin Martin Heidemann<sup>b</sup>,  
Frederik Bernd Laun<sup>c</sup>, Florian Knoll<sup>a</sup>

<sup>a</sup>*Department Artificial Intelligence in Biomedical Engineering (AIBE),  
Friedrich-Alexander-Universität Erlangen-Nürnberg (FAU), Erlangen, Germany*

<sup>b</sup>*Siemens Healthcare AG, Erlangen, Germany*

<sup>c</sup>*Institute of Radiology, University Hospital Erlangen, FAU, Erlangen, Germany*



---

## Abstract

The pursuit of high spatial-angular-temporal resolution for *in vivo* diffusion-weighted magnetic resonance imaging (DW-MRI) at ultra-high field strength (e.g., 7 T) is important in understanding brain microstructure and function. Such pursuit, however, faces several technical challenges. First, increased susceptibility and shorter  $T_2$  relaxation require faster echo train readouts. Second, high angular resolution in  $q$ -space requires the use of high and/or multiple  $b$ -values, which increases noise in diffusion-weighted images and prolongs scan time. Multi-shot interleaved echo-planar imaging (EPI) and advanced reconstruction strategies, e.g., multiplexed sensitivity-encoding (MUSE) and compressed sensing with structured low-rank matrix completion (MUSSELS), have been proven suitable for high-resolution DW-MRI. These methods, however, do not explore complementary  $k$ - $q$ -space sampling and require longer scan time compared to single-shot EPI. To address these challenges, we developed a novel joint reconstruction for multi-shell multi-

band shift-encoding acquisition at 7 T (JETS-EPI). In comparison to MUSE and MUSSELS, it allows for faster acquisition with the use of high inplane acceleration and only two shots per diffusion direction. Moreover, the proposed joint reconstruction exhibits better denoising of DW images and clearer delineation of fiber distributions.

*Keywords:* Diffusion-weighted magnetic resonance imaging, Echo planar imaging, Ultra high field, Joint reconstruction, Low rank, Simultaneous multi slice

---

<sup>1</sup> **1. Introduction**

<sup>2</sup> Diffusion-weighted magnetic resonance imaging (DW-MRI) ([Le Bihan et al., 1986; Merboldt et al., 1985](#)) is a non-invasive modality that is sen-  
<sup>3</sup> sitive to Brownian motion of water molecules. DW-MRI forms the basis for  
<sup>4</sup> diffusion tensor imaging (DTI) ([Basser et al., 1994; Mori et al., 1999](#)) and  
<sup>5</sup> high angular resolution diffusion imaging (HARDI) ([Tuch et al., 2002](#)), and  
<sup>6</sup> has been widely used in acute brain ischemia diagnosis, in tumor detection  
<sup>7</sup> and staging, and in neuroscience 

<sup>8</sup> For DW-MRI acquisition, the commonly used pulse sequence is single-  
<sup>9</sup> shot echo-planar imaging (SS-EPI) ([Mansfield, 1977](#)). SS-EPI is capable  
<sup>10</sup> of rapidly acquiring one DW image per radio-frequency excitation at the  
<sup>11</sup> order of 100 milliseconds, and is thus motion robust. However, conventional  
<sup>12</sup> SS-EPI, even with three-fold accelerated acquisition ([Bammer et al., 2001](#))  
<sup>13</sup> using parallel imaging ([Roemer et al., 1990; Ra and Rim, 1993; Pruessmann et al., 1999; Griswold et al., 2002](#)), still suffers from low spatial resolution  
<sup>14</sup> and geometry distortion.

<sup>15</sup> In the quest for high-spatial-angular-resolution and minimal-geometry-  
<sup>16</sup> distortion DW-MRI, tremendous efforts have been made. Instead of SS-EPI,  
<sup>17</sup> advanced pulse sequences based on multi-shot EPI have been developed, in-  
<sup>18</sup> cluding but not limited to interleaved EPI ([Butts et al., 1993](#)), PROPELLER  
<sup>19</sup> ([Pipe et al., 2002](#)), readout-segmented EPI ([Porter and Heidemann, 2009; Heidemann et al., 2010](#)), and spiral ([Truong and Guidon, 2014](#)). Multi-shot  
<sup>20</sup> EPI acquisition, however, requires not only longer scan time, but also shot-to-  
<sup>21</sup> shot phase variation correction (due to the use of motion-sensitive diffusion  
<sup>22</sup> gradients).

26 The standard shot-to-shot phase variation correction acquires navigator  
27 echoes. To eliminate this, advanced self-navigated image reconstruction tech-  
28 niques have been developed. M<sup>u</sup>ltiplexed sensitivity encoding (MUSE) based  
29 on simultaneous-multi-slice (SMS) (Maudsley, 1980; Breuer et al., 2005) 4-  
30 shot interleaved EPI achieved DW-MRI with sub-millimeter inplane resolu-  
31 tion and maximal  $b$ -value 2000 s/mm<sup>2</sup> at 3 T (Chen et al., 2013). In MUSE,  
32 four shots (i.e., four-fold acceleration per shot) are needed because of two  
33 reasons. First, high spatial resolution requires the use of multi-shot acquisi-  
34 tion. Second, MUSE employs parallel imaging (e.g. SENSE) to reconstruct  
35 shot images for the extraction of shot-to-shot phase variation, a<sup>u</sup>nd four-fold  
36 acceleration per shot is achievable in parallel imaging.

37 Beyond parallel imaging, compressed sensing opens up the possibility of  
38 higher acceleration in MRI (Lustig et al., 2007; Block et al., 2007). Multi-shot  
39 reconstruction techniques based on structured low-rank matrix completion  
40 (MUSSELS) (Mani et al., 2017; Bilgic et al., 2019) achieved 5-shot DW-  
41 MRI with 9-fold acceleration per shot. Recently, joint usage of structured  
42 low-rank constraints and explicit phase mapping (JULEP) (Dai et al., 2022)  
43 incorporated iterative phase update into MUSSELS using 4-shot DW-MRI  
44 with 4-fold acceleration per shot. All these techniques target the recon-  
45 struction of one DW image from interleaved EPI using at least 4 shots, i.e.,  
46 joint- $k$ - $q$ -space acceleration is not explored.

47 Joint- $k$ - $q$ -space acceleration can be achieved via proper regularization  
48 along the diffusion encoding direction. Relevant examples are diffusion ac-  
49 celeration with Gaussian process estimated reconstruction (DAGER) (Wu  
50 et al., 2019) and magnitude-based spatial-angular locally low-rank regular-

51 ization (SPA-LLR) (Hu et al., 2020). DAGER and SPA-LLR address the  
52 reconstruction problem of single-shell diffusion data with  $b$ -values of 1000  
53 and  $2000\text{ s/mm}^2$ , respectively. However, DAGER requires many diffusion  
54 directions, whereas SPA-LLR employs the standard interleaved EPI acqui-  
55 sition (i.e., all DW acquisition shares the same inplane sampling pattern).  
56 Consequently, these techniques still require long acquisition time.

57 In this work, we propose a joint  $k$ - $q$ -slice reconstruction framework for  
58 multi-band multi-shell shift-encoded EPI at 7 T (dubbed as JS-EPI).  
59 First, our acquisition method differs from most existing techniques as it shifts  
60 the  $k$ -space in-plane sampling pattern along the phase encoding ( $k_y$ ) direction  
61 per repetition. Such shifting creates complementary  $k$ - $q$ -space sampling. Sec-  
62 ond, our reconstruction framework generalizes to jointly reconstruct multi-  
63 slice multi-shell multi-direction DW images. This is built upon comprehen-  
64 sive modeling of the acquisition process and construction of regularization  
65 terms (e.g. LLR) as proximal operators. We compared our proposed method  
66 with state-of-the-art multi-shot reconstruction techniques, i.e., MUSE and  
67 MUSSELS, as well as established DW image denoising algorithms, i.e., lo-  
68 cal PCA (Manjón et al., 2013; Veraart et al., 2016). Our proposed method  
69 achieves 7 T three-shell high  $b$ -value (up to  $3000\text{ s/mm}^2$ ) diffusion acquisition  
70 at 1 mm isotropic resolution in less than 23 min.

71 **2. Material and methods**

72 *2.1. Multi-band multi-shell shift-encoded EPI acquisition*

73 Fig. 1 (A) displays an ~~exemplary~~ diffusion weighted image acquisition  
74 ~~using~~ two-shot interleaved EPI. Conventionally, such a sampling pattern is  
75 repeated for all diffusion encoding. In contrast, we propose the  $k_y$ -shifted  
76 diffusion encoding, as shown in Fig. 1 (B). The interleaved EPI sampling  
77 pattern is shifted by one  $k_y$  line between ~~direction~~, with the cycling  
78 period being the acceleration factor per diffusion direction. Fig. 1 (C) dis-  
79 plays an ~~exemplary~~ multi-shell sampling pattern. Every diffusion ~~direction~~ is  
80 distinct from others, thereby constructing a non-colinear sampling pattern.  
81 Such  $k_y$ -shifted non-colinear diffusion encoding exploits complementary  $k$ -  
82  $q$ -space ~~sampling~~. Its benefits are two-fold. First, the  $k_y$ -shifting is linear  
83 and retains consistent echo spacing. Second, DW images share anatomical  
84 structures but differ in image contrast depending on  $b$ -values and diffusion  
85 directions, thus complementary  $q$ -space sampling is well suited for the explo-  
86 ration of structural similarity.

87 *2.2. In vivo acquisition protocols*

88 We implemented multiple in-vivo acquisition protocols at a clinical 7T  
89 MR system (MAGNETOM Terra, Siemens Healthineers, Erlangen, Ger-  
90 many) equipped with a 32-channel head coil (Nova Medical, Wilmington,  
91 MA, USA) and the XR-gradient system (80 mT/m @ 200 T/m/s). To cali-  
92 brate coil sensitivity maps, reference scans employed a gradient-echo (GRE)  
93 sequence.  saturation and mono-polar diffusion-encoding gradients were  
94 used. The phase-encoding direction was selected as anterior-to-posterior.

95 This study was approved by the local ethics committee, and informed con-  
96 sent was obtained before scanning healthy volunteers. Detailed acquisition  
97 parameters are listed below.

98 *2.2.1. Single-shell diffusion acquisition at 1.2 mm isotropic resolution*

99 This protocol employed 220 mm FOV in both read and phase-encoding  
100 directions, base resolution 182mm, 94 slices, bandwidth 1832 Hz/Pixel, echo  
101 spacing 0.75 ms, TE 47 ms, TR 4300 ms, 2 shots per diffusion encoding, in-  
102 plane acceleration 3 as well as partial Fourier 6/8 along the phase-encoding  
103 direction, and multi-band factor 2. This results in  $8.7 \times 2$  fold acceleration  
104 per shot. 30 diffusion directions with  $b$ -value 1000 s/mm<sup>2</sup> and 30 diffusion  
105 directions with  $b$ -value 50 s/mm<sup>2</sup> were acquired at a total scan time of 5'3".  
106 Given the high spatial resolution and the short scan time, this protocol fits  
107 well into clinical studies.

108 *2.2.2. Three-shell diffusion acquisition at 1 mm isotropic resolution*

109 This protocol employed the same FOV, shots, inplane acceleration, and  
110 partial Fourier as Section 2.2.1. Other parameters were base resolution  
111 214 mm, 114 slices, bandwidth 1460 Hz/Pixel, echo spacing 0.81 ms, TE  
112 66 ms, TR 5200 ms, and multi-band factor 3. This results in  $8.7 \times 3$  fold  
113 acceleration per shot. As shown in Fig. 1 (C), three shells were sampled  
114 by 20, 30, 64 diffusion directions with  $b$ -values 1000, 2000, and 3000 s/mm<sup>2</sup>,  
115 respectively.  $b_0$  acquisition was interspersed every ten diffusion directions.  
116 This supplies a total of 126 diffusion directions and 22'25" scan time. This  
117 protocol demonstrates the capabilities of JETS-EPI in achieving high spatial-  
118 angular-temporal resolution and in studying brain microstructure.

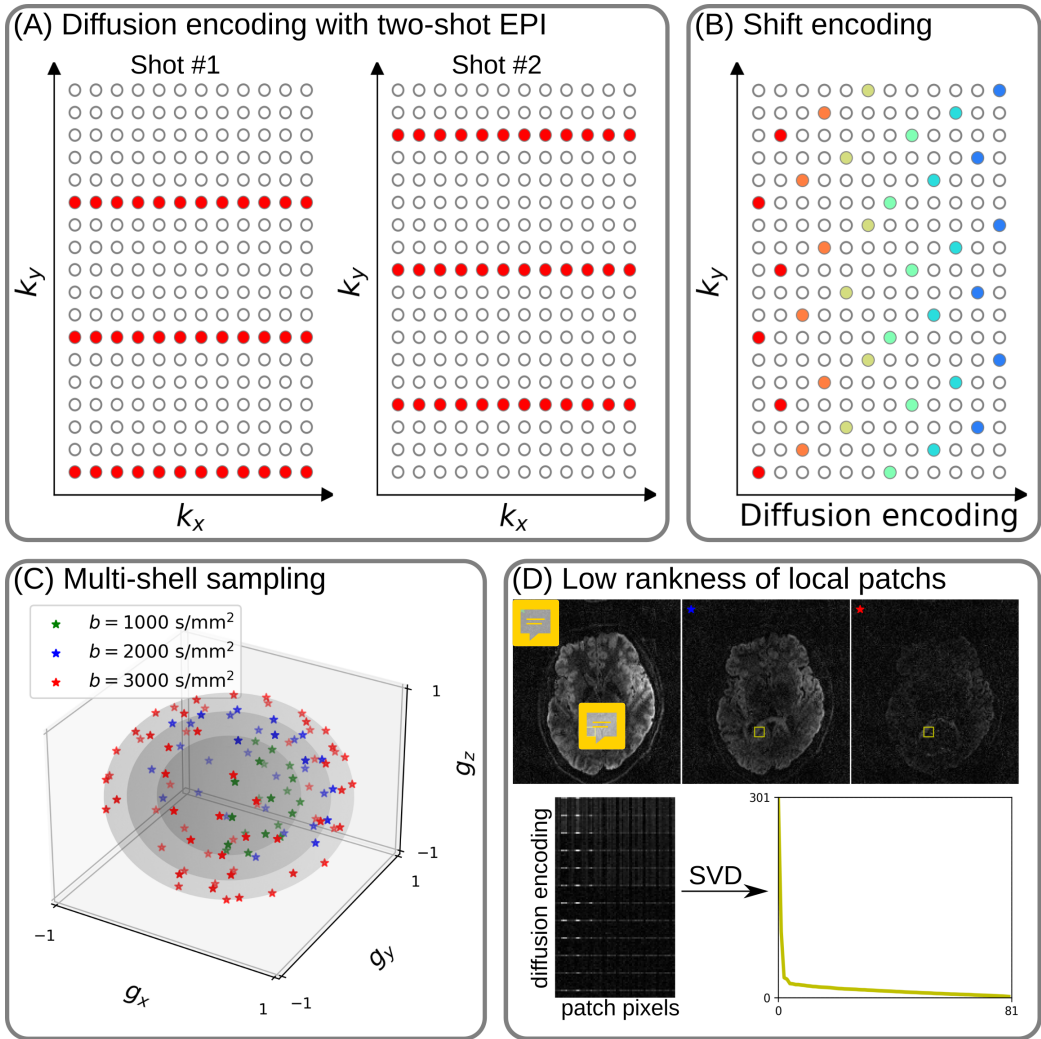


Figure 1: (A) An example DW-MRI acquisition with two-shot interleaved EPI acquisition. (B) The proposed  $k_y$  shifted diffusion encoding scheme. This example employs two shots per DW image. Therefore, every two columns have the same color. (C) An example multi-shell sampling scheme. (D) Low rankness of local image patches (as extracted from the yellow blocks) along multi-shell diffusion encoding.

119 *2.3. Forward modeling*

120 Our proposed acquisition method yields multi-dimensional but slice col-  
121 lapsed  $k$ -space data  $\mathbf{y}_{j,q,s}$ , where  $j, q, s$  denotes the index of the coil sensitivity  
122 map, the diffusion encoding, and the shot, respectively. Such acquisition can  
123 be modeled in two ways.

First, the acquired  $k$ -space data  $\mathbf{y}$  is mapped from individual shot images  
144  $\mathbf{x}_{q,s,z}$  via the forward model,

$$\mathbf{y}_{j,q,s} = \mathbf{P}_{q,s} \boldsymbol{\Sigma} \boldsymbol{\Theta}_z \mathbf{F} \mathbf{S}_j \mathbf{x}_{q,s,z} \quad (1)$$

$$\mathbf{y} := \mathbf{E}_1 \mathbf{x} \quad (2)$$

124 Here, the encoding matrix  $\mathbf{E}_1$  comprises a chain of linear operators. Every  
125 shot image  $\mathbf{x}$  is point-wise multiplied by a set of coil sensitivity maps ( $\mathbf{S}$ ) and  
126 Fourier transformed ( $\mathbf{F}$ ). The output is then point-wise multiplied by the  
127 multi-slice phase map ( $\boldsymbol{\Theta}$ ) with  $z$  the slice index in simultaneously excited  
128 slices. This operator shifts individual slice along the phase-encoding direction  
129 via varying phase modulation (Breuer et al., 2005). The SMS  $k$ -space data  
130 is then summed (collapsed,  $\boldsymbol{\Sigma}$ ) along the slice dimension and masked (point-  
131 wise multiplied,  $\mathbf{P}$ ) by the sampling pattern at every diffusion encoding and  
132 shot.

133 Second, for diffusion MRI based on multi-shot EPI, shot images per dif-  
134 fusion encoding need to be combined as one DW image ( $\tilde{\mathbf{x}}$ ). One method is  
135 to perform magnitude average (Chen et al., 2013) or root-sum-squares (RSS)  
136 (Mani et al., 2017) of shot images. This method is robust to motion, but  
137 sub-optimal with respect to signal-to-noise ratio (SNR) (Guhaniyogi et al.,  
138 2016). Alternatively, shot combination is done via shot-to-shot phase vari-  
139 ation correction (Liu et al., 2005; Chen et al., 2013). This method can be

<sub>140</sub> written as point-wise multiplication between the shot-to-shot phase variation  
<sub>141</sub> ( $\Phi$ ) and the DW image ( $\tilde{\mathbf{x}}$ ),

$$\mathbf{x}_{q,s,z} = \Phi_{q,s,z} \tilde{\mathbf{x}}_{q,z} \quad (3)$$

<sub>142</sub> Note that  $\tilde{\mathbf{x}}$  can be obtained by applying the adjoint of  $\Phi$  to  $\mathbf{x}$ . In MUSE,  
<sub>143</sub>  $\Phi$  is obtained by parallel imaging reconstruction of all shots with subsequent  
<sub>144</sub> phase smoothing of every shot image (e.g. Hanning window). Based on this  
<sub>145</sub> phase correction method, the complete forward model follows

$$\mathbf{y} := \mathbf{E}_2 \tilde{\mathbf{x}} = \mathbf{E}_1 \Phi \tilde{\mathbf{x}} \quad (4)$$

<sub>146</sub> where the encoding matrix  $\mathbf{E}_2$  comprises the chain of the shot-to-shot phase  
<sub>147</sub> variation  $\Phi$  and the encoding matrix  $\mathbf{E}_1$ .

<sub>148</sub> We implemented these two encoding matrices in SigPy ([Ong and Lustig, 2019](#)), utilizing the concept of object-oriented linear operator abstraction.

#### <sub>150</sub> 2.4. Joint $k$ - $q$ -slice reconstruction

<sub>151</sub> Based on the generalized forward models in Eqs. (2) and (4), our proposed  
<sub>152</sub> joint  $k$ - $q$ -slice reconstruction can be formulated as a three-step approach.

<sub>153</sub> I. Joint reconstruction of all shot images by solving the following inverse  
<sub>154</sub> problem with the LLR regularization:

$$\operatorname{argmin}_{\mathbf{x}} \|\mathbf{y} - \mathbf{E}_1 \mathbf{x}\|_2^2 + \lambda \|\mathbf{T} \mathbf{x}\|_* \quad (5)$$

<sub>155</sub> Note that this step suffices in the case of single-shot EPI acquisition.

<sub>156</sub> II. For multi-shot EPI acquisition, shot-to-shot phase variation is extracted  
<sub>157</sub> from  $\mathbf{x}$ . As phase images are spatially smooth ([Chen et al., 2013; Dai](#)

158        et al., 2022), only the central 1/4-FOV  $k$ -space region of  $\mathbf{y}$  is used to  
159        solve for  $\mathbf{x}$ . To obtain shot phases, the reconstructed  $\mathbf{x}$  is interpolated to  
160        the full FOV. The corresponding phase is then filtered by the Hanning  
161        window.

162        III. Joint reconstruction of all DW images using the shot-combined forward  
163        model  $\mathbf{E}_2$  with shot-to-shot phase variation from Step II:

$$\operatorname{argmin}_{\tilde{\mathbf{x}}} \|\mathbf{y} - \mathbf{E}_2 \tilde{\mathbf{x}}\|_2^2 + \lambda \|\mathbf{T} \tilde{\mathbf{x}}\|_* \quad (6)$$

164        *2.5. Locally low rank (LLR) regularization*

165        As shown in Fig. 1 (D), low rankness exists in local patches from multi-  
166        shell DW images. Intuitively, low rankness comes from the contrast variation  
167        feature of DW images. This motivates the application of LLR regularization  
168        (Trzasko and Manduca, 2011; Zhang et al., 2015) for solving the inverse  
169        problems in Eqs. (5) and (6). Here,  $\lambda$  is the regularization strength ( $\lambda \geq 0$ ).  
170         $\mathbf{T}$  represents a linear operator that firstly slides a local patch window through  
171        all DW images and then flattens every set of local patches to two-dimensional  
172        (2D) matrices. The nuclear norm regularization is enforced via singular value  
173        thresholding of all flattened 2D matrices (Cai et al., 2010). We implemented  
174        this regularization term as an proximal operator (Beck, 2017).

175        Noteworthy, it has been reported that LLR is prone to checkerboard  
176        artifacts when  $\lambda$  is too large (Hu et al., 2020). We overcome this problem  
177        utilizing overlapping blocks and provide an efficient implementation. If the  
178        blocks overlap,  $\mathbf{T}^H \mathbf{T}$  input  $\neq$  input, where  $\mathbf{T}^H$  denotes the adjoint operator  
179        of  $\mathbf{T}$ . Our efficient implementation is to scale  $\mathbf{T}^H$  as (1/divisor) $\mathbf{T}^H$ , where  
180        the divisor matrix is obtained by  $\mathbf{T}^H \mathbf{T} \mathbf{1}$ .  $\mathbf{1}$  denotes the matrix of ones with  
181        the same shape as input.

182    2.6. Reconstruction

183    The acquired raw data was read in by twixtools (<https://github.com/pehses/twixtools>). Ramp-sampling regridding and FOV/2-ghost correction were also performed in twixtools. Subsequently, coil sensitivity maps were computed from reference scans using ESPIRiT (Uecker et al., 2014) in SigPy (Ong and Lustig, 2019).

188    With this pre-processing as well as the implemented forward models and  
189    the proximal operator, both inverse problems in Eqs. (5) and (6) were solved  
190    by the alternating direction method of multipliers (ADMM) (Boyd et al.,  
191    2010).

192    ADMM solves the minimization problems in an alternating update scheme,

$$\begin{cases} \mathbf{x}^{(k+1)} := \underset{\mathbf{x}}{\operatorname{argmin}} \| \mathbf{y} - \mathbf{E}(\mathbf{x}) \|_2^2 + \rho/2 \| \mathbf{T}\mathbf{x} - \mathbf{z}^{(k)} + \mathbf{u}^{(k)} \|_2^2 \\ \mathbf{z}^{(k+1)} := \mathcal{T}_{\lambda/\rho}(\mathbf{T}\mathbf{x}^{(k+1)} + \mathbf{u}^{(k)}) \\ \mathbf{u}^{(k+1)} := \mathbf{u}^{(k)} + \mathbf{T}\mathbf{x}^{(k+1)} - \mathbf{z}^{(k+1)} \end{cases} \quad (7)$$

193    where  $k$  denotes the ADMM iteration. Note that  $\mathbf{x}$  can be solved using linear  
194    least square algorithms, e.g. conjugate gradient (Hestenes and Stiefel, 1952),  
195    while  $\mathbf{z}$  is updated via singular value thresholding. The coupling parameter  $\rho$   
196    is effective in both the update of  $\mathbf{x}$  and  $\mathbf{z}$ . It acts as Tikhonov regularization  
197    strength when updating  $\mathbf{x}$ , but also inversely scales the thresholding strength  
198    when updating  $\mathbf{z}$ , ss shown in Supporting Information Figures S1 and S2.

199    In this work, 15 ADMM iterations with  $\rho = 0.05$  and  $\lambda = 0.04$ , and a  
200    block size of 6 for LLR (refer to Supporting Information Figure S3) were  
201    used. All reconstructions were done on a single A100 SXM4/Nvlink GPU  
202    with 40 GB memory (NVIDIA, Santa Clara, CA, USA).

203 We compared our proposed joint reconstruction with established multi-  
204 shot reconstruction techniques, i.e. MUSE (Chen et al., 2013) and MUSSELS  
205 (Mani et al., 2017). We implemented both techniques in Python and vali-  
206 dated them with open-source codes and data (Dai et al., 2022; Bilgic et al.,  
207 2019). For implementation details, please refer to "Reproducing MUSE  
208 and MUSSELS in Python" in the Supporting Information. Further, we de-  
209 noised MUSE diffusion-weighted images with local PCA (Manjón et al., 2013;  
210 Veraart et al., 2016).

211 With reconstructed DW images, fractional anisotropy (FA) maps (Basser  
212 et al., 1994) were fitted using our implementation in Python, whereas fiber  
213 orientation distribution functions (fODF) (Tournier et al., 2007) were com-  
214 puted in DIPY (Garyfallidis et al., 2014).

215 **3. Results**

216 *3.1. Single-shell diffusion acquisition at 1.2 mm isotropic resolution*

217 Fig. 2 displays a DW image for one diffusion direction and zoomed-in  
218 colored FA maps from MUSE, MUSE with denoising, MUSSELS, and JETS  
219 reconstruction. Both MUSE and MUSSELS exhibit residual noise artifacts  
220 for the single-shell acquisition with the  $b$ -value of 1000 s/mm<sup>2</sup>. The local PCA  
221 denoiser removes noise, but the denoised DW image loses fine structures,  
222 e.g. the cuneus (highlighted by the yellow arrow in the figure). This over-  
223 smoothing effect can also be observed in the colored FA map, where the thin  
224 fibers near to gray matter are missing.

225 *3.2. Three-shell diffusion acquisition at 1.0 mm isotropic resolution*

226 Results for a 1.0 mm isotropic resolution three-shell 126-direction diffusion  
227 acquisition are shown in Fig. 3. At this resolution severe reduction of signal-  
228 to-noise ratio (SNR) can be observed for higher  $b$ -values. With such low SNR  
229 levels, brain structures are completely buried below the noise level in MUSE  
230 and MUSSELS. The local PCA denoiser removes noise efficiently from the  
231 reconstructed MUSE images, but images from higher  $b$ -values suffer from  
232 severe blurring that leads to a loss of fine image details. Only the proposed  
233 JETS method with the combination of the  $k_y$ -shift encoding scheme and LLR  
234 regularized reconstruction allows to resolve brain features for higher  $b$ -values.

235 Fig. 4 shows fitted FA maps in three orthogonal orientations based on the  
236 above four DW image reconstruction methods. Corresponding color-coded  
237 FA maps are provided in Supporting Information Figure S6. FA maps from

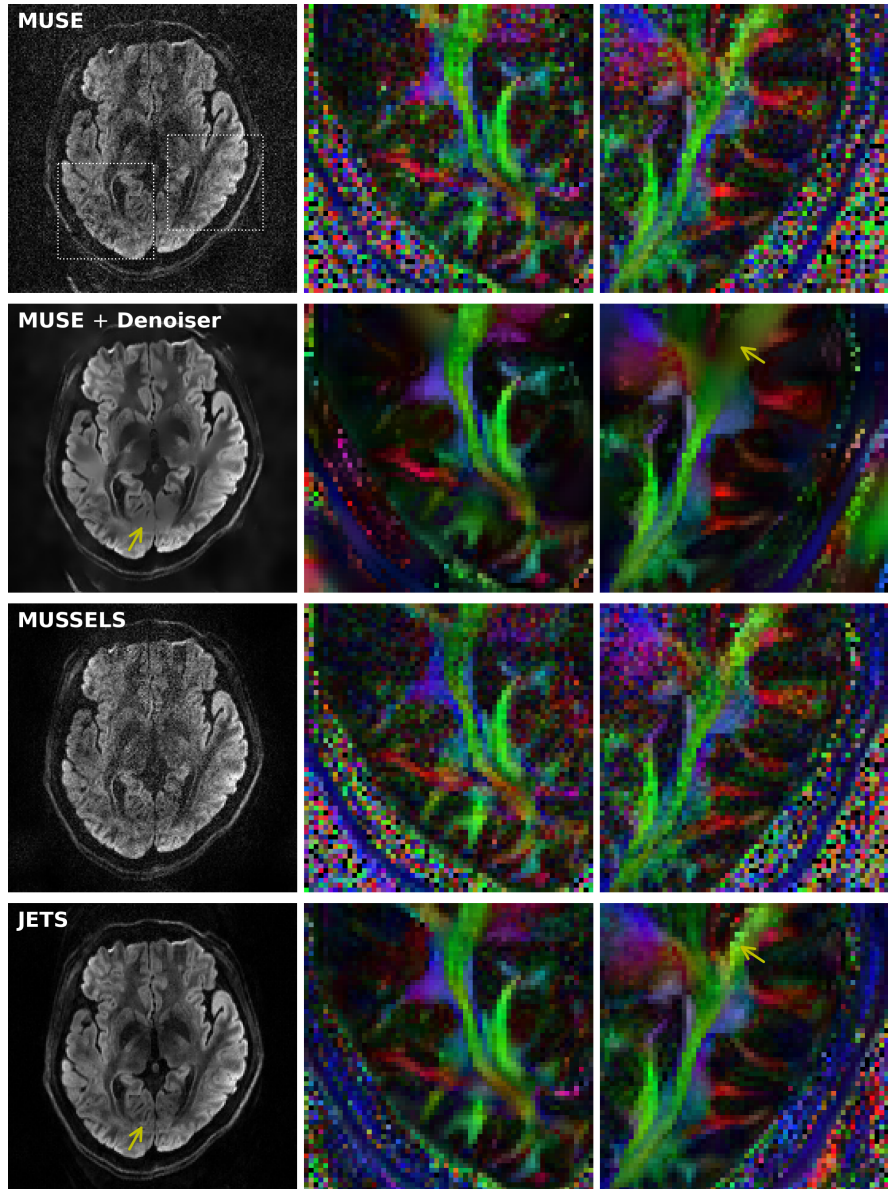


Figure 2: Comparison of reconstructions of a single-shell diffusion acquisition at 1.2 mm isotropic resolution: (1st row) MUSE, (2nd row) MUSE with local PCA denoising, (3rd row) MUSSELS, and (4th row) our proposed JETS approach. The DW image of the 42nd slice and 24th diffusion direction and its zoomed-in colored fractional anisotropy (FA) maps (dashed rectangles) are displayed. The denoiser over-smoothes the images, resulting in missing thin veins and fibers (indicated by yellow arrows).

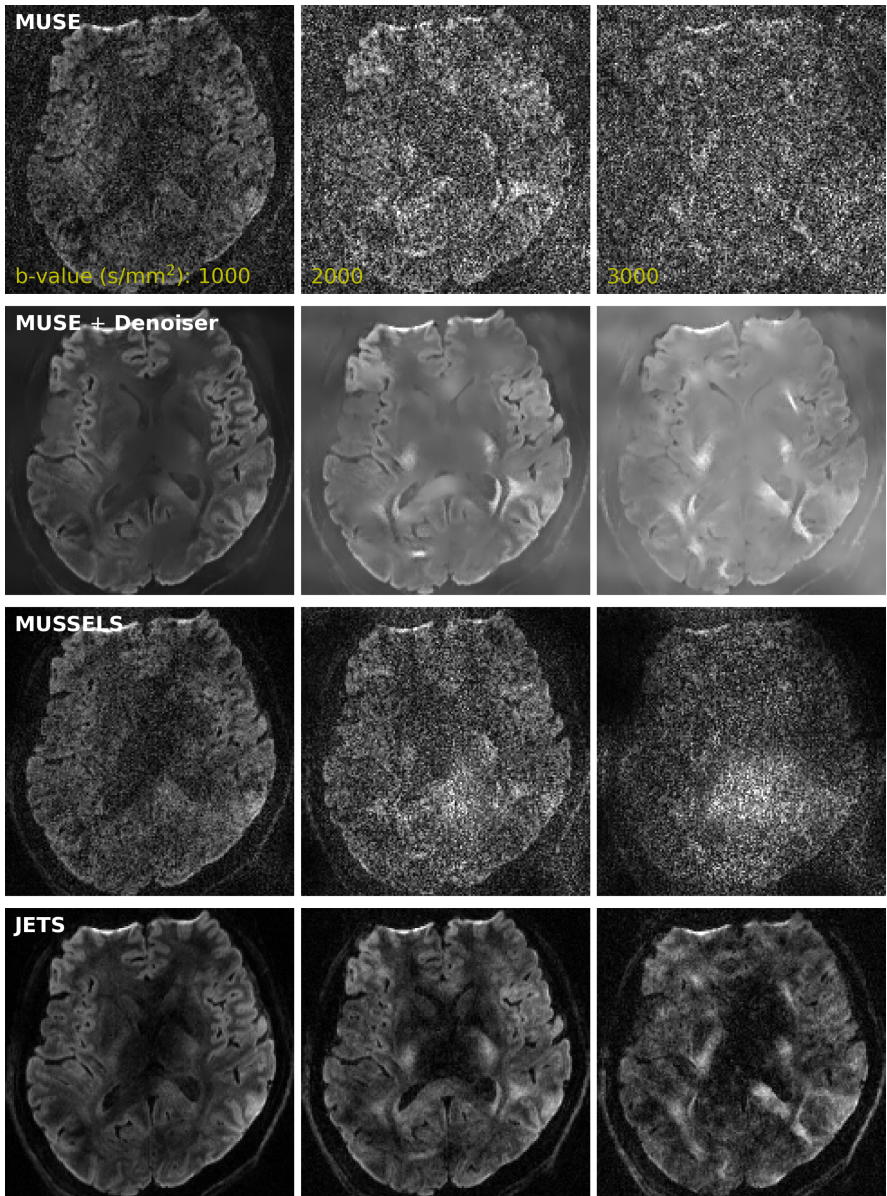


Figure 3: Comparison of reconstructed DW images on three-shell diffusion acquisition at 1 mm isotropic resolution. DW images of the 60th slice for one diffusion direction at different  $b$ -values are displayed: (left) 1000, (center) 2000, and (right) 3000  $\text{s/mm}^2$ .

238 JETS still show better quality and delineate fine details within the putamen  
239 (see white arrows).

240 Fig. 5 shows fODF peaks ([Tournier et al., 2007](#); [Garyfallidis et al., 2014](#))  
241 for the ROIs indicated by the dashed rectangles in the axial and the sagittal  
242 directions in Fig. 4, respectively. These maps provide further insights into  
243 the properties of the evaluated methods.

244 First, noisy DW images from both MUSE and MUSSELS reconstructions  
245 result in chaotic fiber orientation in the axial slice in Fig. 4. The local PCA  
246 denoiser reduces noise in the DW images, but its corresponding fODF peaks  
247 again show over-smoothing effects. In contrast, JETS correctly delineates  
248 crossing fibers in the white matter (indicated by the white arrow). Second,  
249 fODF peaks in mid-sagittal cross-sections of the corpus callosum exhibit  
250 varying fiber densities, which is especially clear in JETS. This shows good  
251 agreement with the established topographical distribution ([Hofer and Frahm,](#)  
252 [2006](#)).

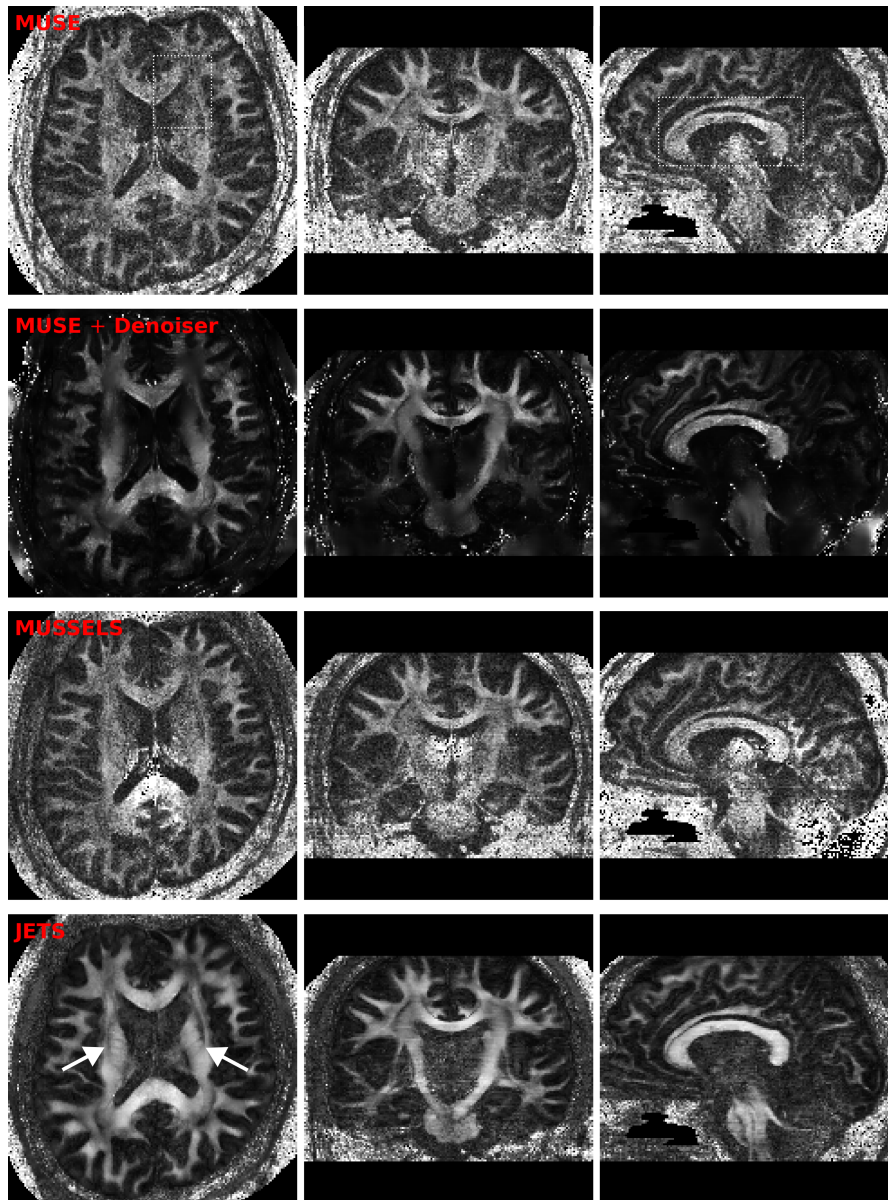


Figure 4: Comparison of reconstructed FA maps based on the 1 mm isotropic resolution three-shell diffusion acquisition. One slice from every orientation (axial, coronal, and sagittal view from left to right) was selected for display.

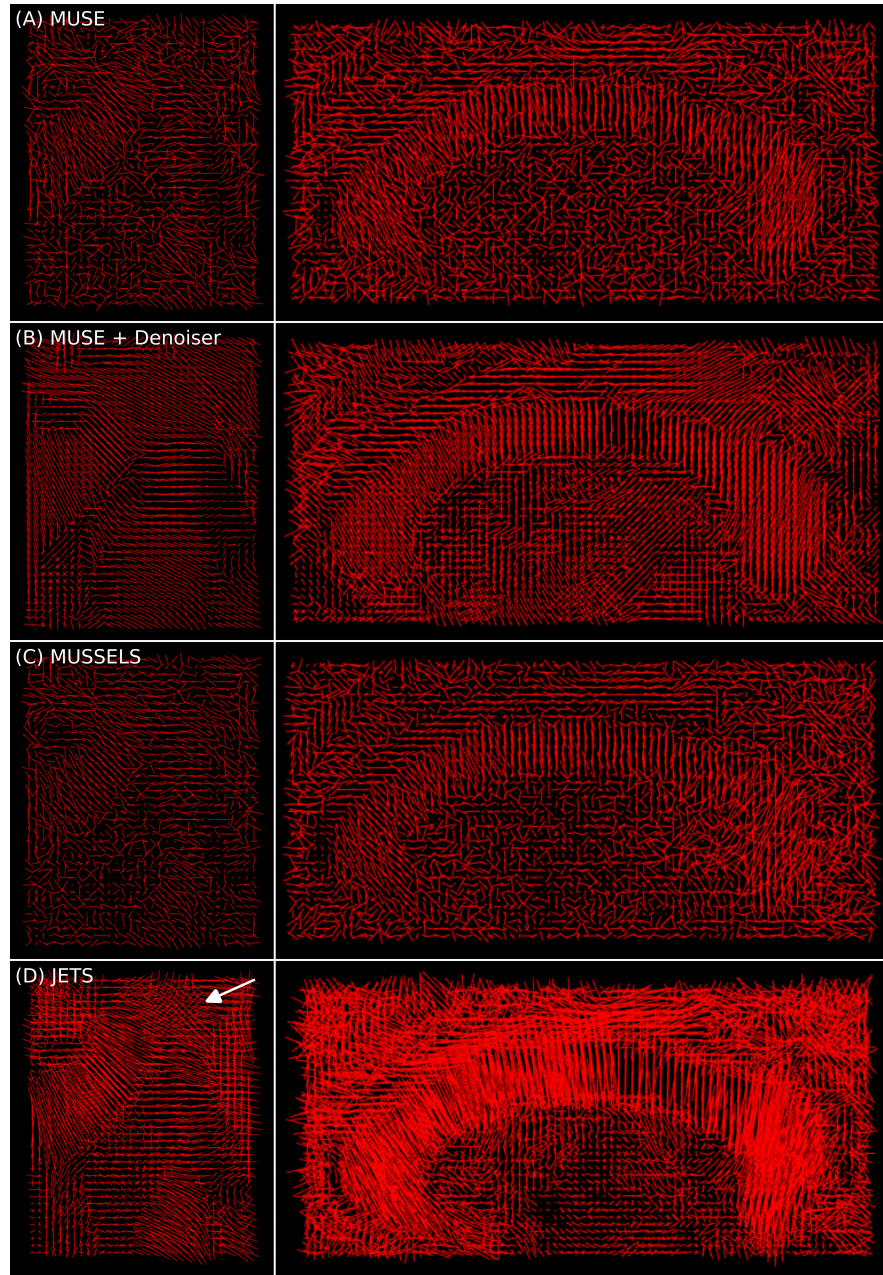


Figure 5: Comparison of fODF peaks within the dashed rectangles of the axial and the sagittal slices in Fig. 4, respectively.

253 **4. Discussion**

254 This work reports a novel DW-MRI technique, dubbed as JETS-EPI,  
255 comprising two ingredients, multi-band  $k_y$ -shift-encoded interleaved EPI for  
256 complementary  $k$ - $q$ -space sampling, and a generalized joint reconstruction  
257 with overlapping locally low-rank regularization to explore low rankness along  
258 the diffusion encoding dimension. JETS-EPI utilizes only two shots per dif-  
259 fusion direction, thereby allowing for short scan time as comparable to single-  
260 shot EPI as well as high spatial resolution with reduced geometric distortion.  
261 Our reconstruction achieves  $8.7 \times 3$  ( $R_{\text{inplane}} \times \text{SMS}$ ) fold accelerated brain  
262 DW-MRI at 7T with 1 mm isotropic resolution and 126 diffusion-direction  
263 (three shells with  $b$ -values of 1000, 2000, and 3000 s/mm<sup>2</sup>) in less than 23 min.

264 The reconstruction results from MUSE and MUSSELS suffer from noise  
265 effects in this study, and the reasons are two-fold. First, the high in-plane  
266 acceleration factor per shot hinders shot-to-shot phase variation estimation  
267 in MUSE, whereas we proposed to jointly reconstruct all shot images from  
268 the central  $k$ -space data. Further, joint reconstruction benefits from the  
269 complementary  $k$ - $q$ -space sampling, as compared to the shot-by-shot parallel  
270 imaging reconstruction. Second, structured low-rank matrix completion as  
271 MUSSELS usually works with at least four shots per diffusion direction,  
272 whereas this study uses only two shots. The use of two shots is beneficial  
273 for shorter scan time than four shots, but hinders the structured low rank  
274 property in MUSSELS.

275 One limitation of JETS-EPI is the long reconstruction time due to the  
276 simultaneous reconstruction of all DW images and the use of overlapping  
277 locally low-rank regularization. The reconstruction on the protocols in Sec-

tion 2.2.1 and Section 2.2.2 takes about 0.5 h and 3 h per collapsed slice, respectively. To reduce the computation time, coil compression algorithms (Huang et al., 2008) can be employed to reduce the number of coils for image reconstruction. Moreover, one may deploy multi-GPU distributed computing or modern optimization algorithms (e.g. stochastic gradient descent) (Ong et al., 2020) to speed up the reconstruction.

## 5. Conclusions

We demonstrated the JETS-EPI technique, which integrates a  $k_y$ -shifted encoding interleaved EPI sequence and a joint reconstruction with overlapping locally low-rank regularization for high spatial-angular-temporal resolution DW-MRI at 7 T. This technique requires no phase navigation, and allows for high quality DW image reconstruction with accelerated acquisition.

## Funding

This work was supported by xxx.

## Data and code available statement

In the spirit of reproducible and open science, we will publish our source code (<https://github.com/ZhengguoTan/sigpy>) as well as the raw  $k$ -space data during the review process.

297 **Acknowledgments**

298     The authors thank the Regionales Rechenzentrum Erlangen (RRZE) and  
299     Zentrum für Nationales Hochleistungsrechnen Erlangen (NHR@FAU) for pro-  
300     viding GPU computational infrastructure.

301 **References**

- 302     Bammer, R., Keeling, S.L., Augustin, M., Pruessmann, K.P., Wolf, R., Stoll-  
303     berger, R., Hartung, H.P., Fazekas, F., 2001. Improved diffusion-weighted  
304     single-shot echo-planar imaging (EPI) in stroke using sensitivity encoding  
305     (SENSE). *Magn. Reson. Med.* 46, 548–554. doi:[10.1002/mrm.1226](https://doi.org/10.1002/mrm.1226).
- 306     Basser, P.J., Mattiello, J., Le Bihan, D., 1994. MR diffusion tensor  
307     spectroscopy and imaging. *Biophys. J.* 66, 259–267. doi:[10.1016/S0006-3495\(94\)80775-1](https://doi.org/10.1016/S0006-3495(94)80775-1).
- 309     Beck, A., 2017. First-order methods in optimization. Society for In-  
310     dustrial and Applied Mathematics, Philadelphia, PA. doi:[10.1137/1.9781611974997](https://doi.org/10.1137/1.9781611974997).
- 312     Bilgic, B., Chatnuntawech, I., Manhard, M.K., Tian, Q., Liao, C., Iyer, S.S.,  
313     Cauley, S.F., Huang, S.Y., Polimeni, J.R., Wald, L.L., Setsompop, K.,  
314     2019. Highly accelerated multishot echo planar imaging through synergistic  
315     machine learning and joint reconstruction. *Magn. Reson. Med.* 82, 1343–  
316     1358. doi:[10.1002/mrm.27813](https://doi.org/10.1002/mrm.27813).
- 317     Block, K.T., Uecker, M., Frahm, J., 2007. Undersampled radial MRI with

- 318 multiple coils. Iterative image reconstruction using a total variation con-  
319 straint. Magn. Reson. Med. 57, 1186–1098. doi:[10.1002/mrm.21236](https://doi.org/10.1002/mrm.21236).
- 320 Boyd, S., Parikh, N., Chu, E., Peleato, B., Eckstein, J., 2010. Distributed  
321 optimization and statistical learning via the alternating direction method  
322 of multipliers. Foundations and Trends in Machine Learning 3, 1–122.  
323 doi:[10.1561/2200000016](https://doi.org/10.1561/2200000016).
- 324 Breuer, F.A., Blaimer, M., Heidemann, R.M., Mueller, M.F., Griswold, M.A.,  
325 Jakob, P.M., 2005. Controlled Aliasing in Parallel Imaging Results in  
326 Higher Acceleration (CAPIRINHA) for Multi-Slice Imaging. Magn. Re-  
327 son. Med. 53, 684–691. doi:[10.1002/mrm.20401](https://doi.org/10.1002/mrm.20401).
- 328 Butts, K., Riederer, S.J., Ehman, R.L., Thompson, R.M., Jack, C.R., 1993.  
329 Interleaved echo planar imaging on a standard MRI system. Magn. Reson.  
330 Med. 31, 67–72. doi:[10.1002/mrm.1910310111](https://doi.org/10.1002/mrm.1910310111).
- 331 Cai, J.F., Candès, E.J., Shen, Z., 2010. A singular value threshold-  
332 ing algorithm for matrix completion. SIAM. J. Optim. 20, 1956–1982.  
333 doi:[10.1137/080738970](https://doi.org/10.1137/080738970).
- 334 Chen, N.K., Guidon, A., Chang, H.C., Song, A.W., 2013. A robust multi-  
335 shot scan strategy for high-resolution diffusion weighted MRI enabled by  
336 multiplexed sensitivity-encoding (MUSE). NeuroImage 72, 41–47. doi:[10.1016/j.neuroimage.2013.01.038](https://doi.org/10.1016/j.neuroimage.2013.01.038).
- 338 Dai, E., Mani, M., McNab, J.A., 2022. Multi-band multi-shot diffusion MRI  
339 reconstruction with joint usage of structured low-rank constraints and ex-  
340 plicit phase mapping. Magn. Reson. Med. doi:[10.1002/mrm.29422](https://doi.org/10.1002/mrm.29422).

- 341 Garyfallidis, E., Brett, M., Amirbekian, B., Rokem, A., van der Walt, S.,  
342 Descoteaux, M., Nimmo-Smith, I., Contributors, D., 2014. DIPY, a library  
343 for the analysis of diffusion MRI data. *Front. Neuroinform.* 8, 1–17. doi:[10.3389/fninf.2014.00008](https://doi.org/10.3389/fninf.2014.00008).
- 345 Griswold, M.A., Jakob, P.M., Heidemann, R.M., Nittka, M., Jellus, V.,  
346 Wang, J., Kiefer, B., Haase, A., 2002. Generalized autocalibrating par-  
347 tially parallel acquisitions (GRAPPA). *Magn. Reson. Med.* 47, 1202–1210.  
348 doi:[10.1002/mrm.10171](https://doi.org/10.1002/mrm.10171).
- 349 Guhaniyogi, S., Chu, M.L., Chang, H.C., Song, A.W., Chen, N.K., 2016. Mo-  
350 tion immune diffusion imaging using augmented MUSE for high-resolution  
351 multi-shot EPI. *Magn. Reson. Med.* 75, 639–652. doi:[10.1002/mrm.25624](https://doi.org/10.1002/mrm.25624).
- 352 Heidemann, R.M., Porter, D.A., Anwander, A., Feiweier, T., Heberlein, K.,  
353 Knösche, T.R., Turner, R., 2010. Diffusion imaging in humans at 7 T  
354 using readout-segmented EPI and GRAPPA. *Magn. Reson. Med.* 64, 9–  
355 14. doi:[10.1002/mrm.22480](https://doi.org/10.1002/mrm.22480).
- 356 Hestenes, M.R., Stiefel, E., 1952. Methods of conjugate gradients for solving  
357 linear systems. *J. Res. Natl. Bur. Stand.* 49, 409–436. doi:[10.6028/jres.049.044](https://doi.org/10.6028/jres.049.044).
- 359 Hofer, S., Frahm, J., 2006. Topography of the human corpus callosum revis-  
360 ited – Comprehensive fiber tractography using diffusion tensor magnetic  
361 resonance imaging. *NeuroImage* 32, 989–994. doi:[10.1016/j.neuroimage.2006.05.044](https://doi.org/10.1016/j.neuroimage.2006.05.044).

- 363 Hu, Y., Wang, X., Tian, Q., Yang, G., Daniel, B., McNab, J., Hargreaves, B.,  
364 2020. Multi-shot diffusion-weighted MRI reconstruction with magnitude-  
365 based spatial-angular locally low-rank regularization (SPA-LLR). Magn.  
366 Reson. Med. 83, 1596–1607. doi:[10.1002/mrm.28025](https://doi.org/10.1002/mrm.28025).
- 367 Huang, F., Vijayakumar, S., Li, Y., Hertel, S., Duensing, G.R., 2008. A soft-  
368 ware channel compression technique for faster reconstruction with many  
369 channels. Magn. Reson. Imaging 26, 133–141.
- 370 Le Bihan, D., Breton, E., Lallemand, D., Grenier, P., Cabanis, E., Laval-  
371 Jeantet, M., 1986. MR imaging of intravoxel incoherent motions: appli-  
372 cation to diffusion and perfusion in neurologic disorders. Radiology 161,  
373 401–407. doi:[10.1148/radiology.161.2.3763909](https://doi.org/10.1148/radiology.161.2.3763909).
- 374 Liu, C., Moseley, M.E., Bammer, R., 2005. Simultaneous phase cor-  
375 rection and SENSE reconstruction for navigated multi-shot DWI with  
376 non-Cartesian  $k$ -space sampling. Magn. Reson. Med. 54, 1412–1422.  
377 doi:[10.1002/mrm.20706](https://doi.org/10.1002/mrm.20706).
- 378 Lustig, M., Donoho, D., Pauly, J.M., 2007. Sparse MRI: The application of  
379 compressed sensing for rapid MR imaging. Magn. Reson. Med. 58, 1182–  
380 1195. doi:[10.1002/mrm.21391](https://doi.org/10.1002/mrm.21391).
- 381 Mani, M., Jacob, M., Kelley, D., Magnotta, V., 2017. Multi-shot sensitivity-  
382 encoded diffusion data recovery using structured low-rank matrix comple-  
383 tion (MUSSELS). Magn. Reson. Med. 78, 494–507. doi:[10.1002/mrm.26382](https://doi.org/10.1002/mrm.26382).

- 385 Manjón, J.V., Coupé, P., Concha, L., Buades, A., Collins, D.L., Robles, M.,  
386 2013. Diffusion weighted image denoising using overcomplete local PCA.  
387 PLoS One 8, e73021. doi:[10.1371/journal.pone.0073021](https://doi.org/10.1371/journal.pone.0073021).
- 388 Mansfield, P., 1977. Multi-planar image formation using NMR spin echoes.  
389 J Phys C 10, 55–58. doi:[10.1088/0022-3719/10/3/004](https://doi.org/10.1088/0022-3719/10/3/004).
- 390 Maudsley, A.A., 1980. Multiple-line-scanning spin density imaging. J. Magn.  
391 Reson. 41, 112–126. doi:[10.1016/0022-2364\(80\)90207-3](https://doi.org/10.1016/0022-2364(80)90207-3).
- 392 Merboldt, K.D., Hanicke, W., Frahm, J., 1985. Self-diffusion NMR imag-  
393 ing using stimulated echoes. J. Magn. Reson. 64, 479–486. doi:[10.1016/0022-2364\(85\)90111-8](https://doi.org/10.1016/0022-2364(85)90111-8).
- 395 Mori, S., Crain, B.J., Chacko, V.P., Van Zijl, P.C.M., 1999. Three-  
396 dimensional tracking of axonal projections in the brain by mag-  
397 netic resonance imaging. Ann. Neurol. 45, 265–269. doi:[10.1002/1531-8249\(199902\)45:2<265::AID-ANA21>3.0.CO;2-3](https://doi.org/10.1002/1531-8249(199902)45:2<265::AID-ANA21>3.0.CO;2-3).
- 399 Ong, F., Lustig, M., 2019. SigPy: A Python package for high performance  
400 iterative reconstruction, in: Proceedings of the 27th Annual Meeting of  
401 ISMRM, Montréal, CAN, p. 4819.
- 402 Ong, F., Zhu, X., Cheng, J.Y., Johnson, K.M., Larson, P.E.Z., Vasanawala,  
403 S.S., Lustig, M., 2020. Extreme MRI: Large-scale volumetric dynamic  
404 imaging from continuous non-gated acquisitions. Magn. Reson. Med. 84,  
405 1763–1780. doi:[10.1002/mrm.28235](https://doi.org/10.1002/mrm.28235).
- 406 Pipe, J.G., Farthing, V.G., Forbes, K.P., 2002. Multishot diffusion-weighted

- 407 FSE using PROPELLER MRI. Magn. Reson. Med. 47, 42–52. doi:[10.1002/mrm.10014](https://doi.org/10.1002/mrm.10014).
- 408
- 409 Porter, D.A., Heidemann, R.M., 2009. High resolution diffusion-weighted  
410 imaging using readout-segmented echo-planar imaging, parallel imaging  
411 and a two-dimensional navigator-based reacquisition. Magn. Reson. Med.  
412 62, 468–475. doi:[10.1002/mrm.22024](https://doi.org/10.1002/mrm.22024).
- 413 Pruessmann, K.P., Weiger, M., Scheidegger, M.B., Boesiger, P., 1999.  
414 SENSE: Sensitivity encoding for fast MRI. Magn. Reson. Med. 42, 952–  
415 962. doi:[10.1002/\(SICI\)1522-2594\(199911\)42:5<952::AID-MRM16>3.0.CO;2-S](https://doi.org/10.1002/(SICI)1522-2594(199911)42:5<952::AID-MRM16>3.0.CO;2-S).
- 416
- 417 Ra, J.B., Rim, C.Y., 1993. Fast imaging using subencoding data sets from  
418 multiple detectors. Magn. Reson. Med. 30, 142–145. doi:[10.1002/mrm.1910300123](https://doi.org/10.1002/mrm.1910300123).
- 418
- 419
- 420 Roemer, P.B., Edelstein, W.A., Hayes, C.E., Souza, S.P., Mueller, O.M.,  
421 1990. The NMR phased array. Magn. Reson. Med. 16, 192–225. doi:[10.1002/mrm.1910160203](https://doi.org/10.1002/mrm.1910160203).
- 421
- 422
- 423 Tournier, J.D., Calamante, F., Connelly, A., 2007. Robust determination  
424 of the fibre orientation distribution in diffusion MRI: Non-negativity con-  
425 strained super-resolved spherical deconvolution. NeuroImage 35, 1459–  
426 1472. doi:[10.1016/j.neuroimage.2007.02.016](https://doi.org/10.1016/j.neuroimage.2007.02.016).
- 426
- 427 Truong, T.K., Guidon, A., 2014. High-resolution multishot spiral diffusion  
428 tensor imaging with inherent correction of motion-induced phase errors.  
429 Magn. Reson. Med. 71, 790–796. doi:[10.1002/mrm.24709](https://doi.org/10.1002/mrm.24709).

- 430 Trzasko, J., Manduca, A., 2011. Local versus global low-rank promotion in  
431 dynamic MRI series reconstruction, in: Proceedings of the 19th Annual  
432 Meeting of ISMRM, Montréal, CAN, p. 4371.
- 433 Tuch, D.S., Reese, T.G., Wiegell, M.R., Makris, N., Belliveau, J.W., Wedeen,  
434 V.J., 2002. High angular resolution diffusion imaging reveals intravoxel  
435 white matter fiber heterogeneity. Magn. Reson. Med. 48, 577–582. doi:[10.1002/mrm.10268](#).
- 437 Uecker, M., Lai, P., Murphy, M.J., Virtue, P., Elad, M., Pauly, J.M.,  
438 Vasanawala, S.S., Lustig, M., 2014. ESPIRiT – an eigenvalue approach  
439 to autocalibrating parallel MRI: Where SENSE meets GRAPPA. Magn.  
440 Reson. Med. 71, 990–1001. doi:[10.1002/mrm.24751](#).
- 441 Veraart, J., Novikov, D.S., Christiaens, D., Ades-aron, B., Sijbers, J., Fiere-  
442 mans, E., 2016. Denoising of diffusion mri using random matrix theory.  
443 NeuroImage 142, 394–406. doi:[10.1016/j.neuroimage.2016.08.016](#).
- 444 Wu, W., Koopmans, P.J., Andersson, J.L., Miller, K.L., 2019. Diffusion  
445 Acceleration with Gaussian process Estimated Reconstruction (DAGER).  
446 Magn. Reson. Med. 82, 107–125. doi:[10.1002/mrm.27699](#).
- 447 Zhang, T., Pauly, J.M., Levesque, I.R., 2015. Accelerated parameter mapping  
448 with a locally low rank constraint. Magn. Reson. Med. 73, 655–661. doi:[10.1002/mrm.25161](#).